Constraining the Distribution of 3D Fractal Structures in Mud Flocs

Thesis by
Brayden Noh

In Partial Fulfillment of the Requirements for the
Degree of
Bachelor of Science

CALIFORNIA INSTITUTE OF TECHNOLOGY
Pasadena, California

2025
Defended 6/4/2025

Brayden Noh
ORCID: 0000-0002-4526-0717

ACKNOWLEDGEMENTS

I am deeply grateful to Professor Michael Lamb, my thesis advisor, research advisor, and mentor, for introducing me to geomorphology, sedimentology, and the excitement of research since my freshman year. His guidance and enthusiasm have shaped both my academic journey and my approach to scientific inquiry.

I would also like to thank my collaborators in the group: Dr. Kieran Dunne, Dr. Omar Wani, Dr. Kimberly Miller, Dr. Justin Nghiem, Dr. Dongchen Wang, and Dr. Yutian Ke. Each of them provided remarkable patience, generosity, and encouragement throughout my undergraduate years. Their insight and support have been invaluable to this work.

This research was supported by the NASA FINESST Grant 80NSSC20K1645, the NASA Delta-X project funded by the Science Mission Directorate's Earth Science Division through the Earth Venture Suborbital-3 Program NNH17ZDA001N-EVS3, and the National Science Foundation Geomorphology and Land-use Dynamics Grant No. 2136991. I gratefully acknowledge this funding, which made my research possible. I also thank Nick Andersen for helping to build the floc mill.

Finally, and most importantly, I am grateful to my family for their unwavering support for exploring my curiosity

ABSTRACT

Mud builds coastal landscapes and governs the long-term evolution of river deltas, floodplains, and estuaries, yet predicting its transport remains difficult because mud aggregates into flocs with complex, fractal structures that deviate from simple particle behavior. The three-dimensional (3D) fractal dimension of these flocs sets their settling and sediment transport characteristics, but reliably determining this parameter across diverse environments is a persistent challenge. Conventional aggregation of floc data often obscures real structural diversity and can yield misleading fractal dimensions due to Simpson's Paradox. This study tests the hypothesis that stratifying settling data by image-derived two-dimensional (2D) fractal dimension enables more accurate inference of the hydrodynamically relevant 3D fractal dimension. Controlled experiments with freshwater flocs, formed under varied shear and particulate organic matter (POM) conditions, were conducted using in-situ imaging, PIV-corrected tracking, and box-counting analysis to resolve structural differences. Results demonstrate that aggregation overestimates the 3D fractal dimension, while stratification reveals clear trends: the inferred 3D fractal dimension increases with shear stress and decreases with particulate organic matter content. These findings provide a basis for more realistic floc modeling and improve predictions of fine sediment transport.

TABLE OF CONTENTS

LIST OF ILLUSTRATIONS

LIST OF TABLES

NOMENCLATURE

μ. Dynamic viscosity [Pa·s].

ν. Kinematic viscosity [m^2/s].

ρ_f. Fluid density [kg/m^3].

ρ_p. Particle density [kg/m^3].

A. Area [m^2].

b_1. Shape (drag) factor [–].

d. Particle diameter [m].

d_f. Floc diameter [m].

d_p. Primary particle diameter [m].

g. Gravitational acceleration [m/s^2].

N. Number of primary particles in a floc [–].

n_f. Fractal dimension (2D or 3D, context-dependent) [–].

P. Perimeter [m].

R_f. Floc submerged specific gravity [–].

R_s. Primary particle submerged specific gravity [–].

u_*. Shear velocity [m/s].

w_s. Settling velocity [m/s].

Chapter 1

INTRODUCTION

Mud, characterized by particles smaller than 62.5 microns, constitutes over 80% of the sediment load in most rivers and is the primary component of deposition in lowland and deltaic environments (Kranenburg, 1994; Lamb et al., 2020; T. Healy, Y. Wang, and J.-A. Healy, 2002). Understanding the transport and fate of fine-grained sediment is thus crucial for modeling the long-term evolution of deltas, floodplains, and estuaries (Winterwerp, 2002; Kranenburg, 1994; Nghiem et al., 2022; Lamb et al., 2020). Accurate predictions of fine sediment dynamics are also critical for water quality management (Droppo et al., 1997), contaminant transport (Liss et al., 1996), and for the design of effective river and coastal restoration strategies (Esposito et al., 2017; Kemp et al., 2016). Furthermore, mud plays a central role in the global carbon cycle, with fine-grained mineral surfaces offering reactive sites for the adsorption and preservation of organic carbon (Bianchi et al., 2024).

The settling dynamics of suspended particles fundamentally control the processes of mud deposition in rivers and estuaries. Many predictive approaches for sediment transport begin with Stokes' law, which describes the terminal settling velocity (w_s) of smooth, impermeable spheres at low Reynolds numbers (Stokes et al., 1851; Bird, 2006):

$$w_s = \frac{g(\rho_p - \rho_f)d^2}{18\mu} \tag{1.1}$$

where g is gravitational acceleration, ρ_p and ρ_f are the densities of the particle and fluid, d is particle diameter, and μ is dynamic viscosity. Stokes' law reliably describes the settling of isolated spheres; however, applying it to fine-grained sediment produces predictions that conflict with field observations. For instance, using the law for a single 1 μm mud particle in a 5 m-deep river flowing at 1 m, s^{-1} yields a settling velocity of only 9×10^{-8} m, s^{-1}, implying a deposition time of more than 600 days. During that time, the particle would be transported over 55,000 km downstream. However, this theoretical calculation stands in contrast to several field observations. For example, lowland rivers are often bordered by levees actively built by overbank flows, with many of these levees composed of mud, some containing high clay content (e.g., 50%) (Aalto, Lauer, and Dietrich, 2008). Additionally, deposition rates on alluvial ridges decline exponentially away from the channel, implying transport lengths of tens to hundreds of meters, rather than tens of kilometers (Hajek and Wolinsky, 2012).

These observed transport and deposition patterns indicate that mud in rivers settles much faster than predicted for individual, isolated particles. This deviation arises because suspended mud particles do not remain isolated but rapidly undergo flocculation to form larger, composite aggregates that settle more quickly than their individual constituents (Kranenburg, 1994; Johnson, X. Li, and Logan, 1996; I. G. Droppo, 2001). However, these aggregates are not the dense, impermeable spheres assumed by Stokes' law. Instead, they are highly porous, open structures whose effective density decreases as their size increases (Meakin, 1992; Kranenburg, 1994). It is well established that such aggregates tend to be self-similar and fractal in structure (Family and Landau, 2012; Jullien, 1987). The hierarchical organization of flocs is effectively captured by a simple scaling law derived from fractal theory (Meakin, 1992). Specifically, the relationship between floc mass and size follows:

$$N \sim \left(\frac{d_f}{d_p}\right)^{n_f} \tag{1.2}$$

where N is the number of primary particles, d_f is the floc diameter, d_p is the primary particle diameter, and n_f is the fractal dimension. Building on this, Kranenburg (1994) showed that the solid volume fraction, and thus the excess density, of a floc decreases as a power law with increasing floc size:

$$R_f = R_s \left(\frac{d_f}{d_p}\right)^{n_f - 3} \tag{1.3}$$

where R_f is the floc's submerged specific gravity, R_s is that of the primary particles, d_f is floc diameter, d_p is primary particle diameter, and n_f is the three-dimensional fractal dimension. Submerged specific gravity is defined generally as $(\rho - \rho_f)/\rho_f$, where ρ is the density of the particle and ρ_f is the fluid density.

Substituting this fractal scaling of excess density into Stokes' law for a floc, and expressing viscosity in terms of the kinematic viscosity ($\nu = \mu/\rho$), yields the explicit fractal floc settling velocity equation (Strom and Keyvani, 2011):

$$w_s = \frac{g R_s}{b_1 \nu d_p^{n_f - 3}} \, d_f^{n_f - 1} \tag{1.4}$$

where b_1 is a shape factor that generalizes the original Stokes constant of 18 for spheres. For natural sediments, which are irregular, porous, and often non-spherical,

b_1 serves as an empirical correction factor to account for deviations from idealized behavior (Ferguson and Church, 2004). This implies that the exponent in the velocity–diameter relation is directly set by the fractal dimension, with $w_s \propto d_f^{n_f - 1}$ for a fixed d_p (Johnson, X. Li, and Logan, 1996; D. H. Li and Ganczarczyk, 1989). Consequently, the slope of a log–log plot of settling velocity versus floc diameter provides a direct estimate of the aggregate fractal dimension.

However, this application rests on the implicit assumption that all flocs in the population share a single, well-defined fractal dimension. In reality, floc populations are heterogeneous: aggregate growth and breakup are influenced by factors such as organic matter content, turbulence, and hydrodynamic conditions, leading to a broad spectrum of floc structures and fractal dimensions (Nghiem et al., 2022). This heterogeneity presents a fundamental challenge for settling theory. In a mixed population containing flocs with diverse fractal dimensions, a single power-law fit to bulk measurements may obscure the underlying structural variability.

To illustrate how structural heterogeneity influences settling behavior, consider a mixed population of flocs composed of three subgroups with distinct true fractal dimensions: $n_f = 1.5$, 2.0, and 2.5. Each group is assumed to have the same primary particle diameter, $d_p = 10^{-5}$ m, which is indicated by the arrow in Fig. 1.1. According to Eq. (1.4), the slope of the log–log relationship between settling velocity and floc diameter for each group is given by $n_f - 1$. Therefore, when each n_f subgroup is analyzed separately, their respective log–log slopes are 0.5, 1.0, and 1.5, as illustrated in Fig. 1.1.

A paradoxical situation can arise, however, if these distinct n_f subgroups are aggregated and analyzed as a single dataset. If, within this pooled dataset, floc diameter (d_f) exhibits a positive correlation with the 3D fractal dimension (n_f), then fitting a single power-law relationship to the aggregated data can yield a substantially skewed and misleading exponent. In the toy scenario in Fig. 1.1, an aggregated log–log slope of 2 (implying an effective $n_f = 3$) is observed, equal to the settling behavior of a smooth, impermeable sphere.

This outcome exemplifies Simpson's Paradox (Simpson, 1951), a statistical phenomenon in which trends or relationships observed within individual subgroups are reversed, masked, or distorted when those subgroups are aggregated. In the context of floc settling, this means that combining data from structurally diverse floc populations can yield misleading global relationships that do not reflect the true behavior of any subgroup. In our context, the aggregated slope fails to accurately

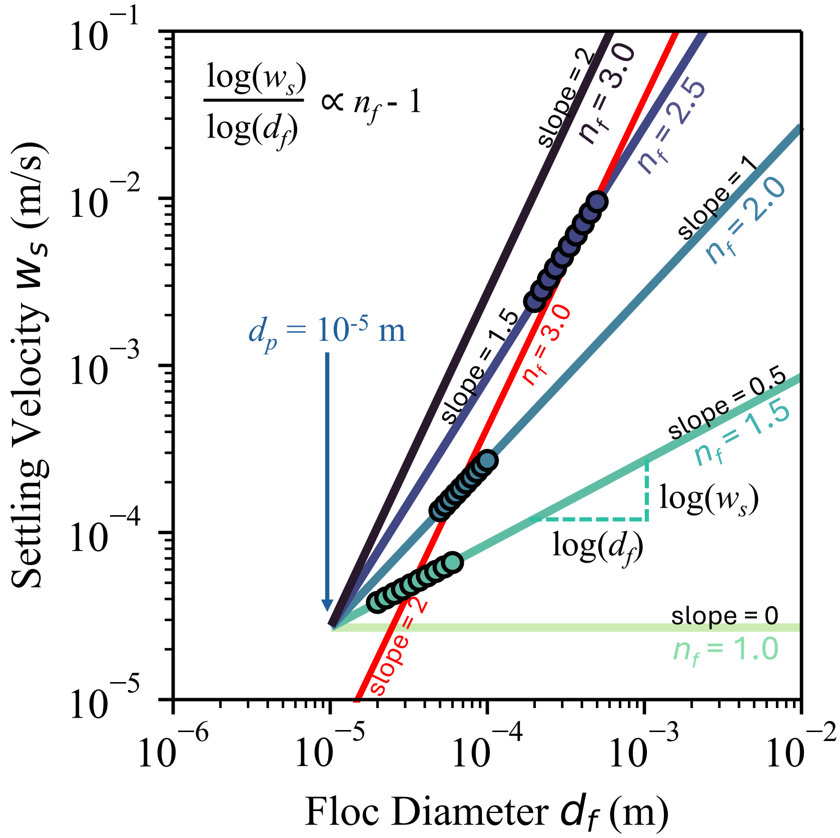

Figure 1.1: Toy model illustrating Simpson's Paradox: Three floc groups (n_f = 1.5, 2.0, 2.5) with the same d_p yield distinct slopes when fit separately, but their aggregated data converge to a slope of 2, matching an impermeable sphere and masking subgroup variability.

reflect the settling behavior of any single fractal dimension class (all of which have $n_f \leq 2.5$), because n_f functions as a confounding variable. When larger diameters systematically coincide with higher fractal dimensions, the global regression captures a spurious trend that does not represent the true behavior of any constituent group. As a result, the distinct physical behaviors of each n_f subgroup are lost, and any interpretation of the aggregate slope as a universal settling law for these flocs becomes statistically and physically misleading.

To estimate fractal dimension independently of settling dynamics, many studies have employed image-based techniques that analyze *in situ* two-dimensional (2D) projections of flocs (Jarvis, Jefferson, and Parsons, 2005). These methods typically calculate a 2D fractal dimension from high-resolution images and then infer the corresponding three-dimensional (3D) structure using empirical or simulation-based relationships. A common strategy involves relating the perimeter–area scaling of projected flocs to a 2D fractal dimension, and then using synthetic or computationally generated aggregates to derive a functional relationship between the 2D and 3D fractal dimensions (Maggi and J. Winterwerp, 2004; Lee and Kramer, 2004; Tang and Federico Maggi, 2015). However, the physical relevance of such projection-based approaches for experimental flocs is inherently limited. The relationship between 2D and 3D fractal dimensions is established using synthetic aggregates, which may not fully replicate the aggregation dynamics or structural variability of natural or experimental flocs. As a result, image-based techniques can introduce systematic structural biases and may not yield accurate estimates of the true 3D fractal dimension in real-world floc populations.

To overcome these limitations, we introduce a hybrid approach that links image-based structure with settling dynamics by stratifying the floc population into groups based on their 2D box-counting fractal dimension. For each group, we perform a separate regression of settling velocity against floc diameter, enabling inference of a hydrodynamically relevant 3D fractal dimension for each structural subgroup. This stratification preserves internal variability and reduces Simpson-type aggregation bias, ultimately yielding more accurate estimates of parameters for floc transport modeling.

We evaluated the approach in controlled laboratory experiments that systematically varied shear velocity and organic-matter concentration. High-resolution *in-situ* imaging captured detailed floc morphologies and settling trajectories. The work pursued three objectives: (1) demonstrate structurally distinct subgroups within the floc population, each exhibiting a unique fractal dimension; (2) relate 2-D image–derived fractal dimensions to settling-inferred 3-D dimensions and validate that relationship against theoretical models; and (3) estimate the effective primary particle size (d_p) and quantify how the shape factor (b_1) varies with the 3-D fractal dimension (n_f).

This paper first describes the experimental design and measurement techniques for quantifying floc size, shape, and settling behavior. Next, we outline the image-processing procedures used to extract structural descriptors from 2D projections. Finally, we present an analytical framework that links these descriptors to settling dynamics, refining our understanding of floc structure–function relationships in natural and engineered systems.

Chapter 2

METHODOLOGY

This chapter outlines the experimental design, data acquisition, and analytical procedures used to quantify the structure and settling behaviour of suspended flocs under controlled laboratory conditions. First, the flocculation tank and imaging system—designed to measure floc size, shape, and velocity under adjustable shear—are described. The experimental protocols, including mineral composition, shear-velocity settings, and organic-matter additions, are then detailed. Subsequent sections present the image-processing workflow that extracts floc properties from high-resolution video, along with the corrections applied to isolate gravitational settling and compute equivalent diameters.

To interpret the settling data, the system is calibrated with reference materials, and fractal-scaling models are applied to obtain floc fractal dimensions. Several complementary methods are introduced for estimating two-dimensional (2-D) and three-dimensional (3-D) fractal dimensions, including box-counting analysis and slope-based inference from power-law regressions. Finally, a procedure for estimating the primary-particle diameter (d_p) is presented, based on the intersection of log–log regressions obtained for floc subpopulations that differ in fractal structure. Together, these methods provide the basis for analysing how structural heterogeneity governs floc settling dynamics.

2.1 Experimental Setup

We performed flocculation experiments in a custom mixing tank designed to maintain controlled laboratory conditions (Fig. 2.1a). The tank comprises a cylindrical PVC pipe, 20 cm in diameter and 60 cm tall, filled with water to a depth of 40 cm. A motor-driven paddle, mounted above the open top and submerged just below the free surface, sets the desired shear. Shear velocity, u_*, was empirically calibrated for each run by converting motor revolutions per minute to u_* using a relationship derived from previous sediment-entrainment trials in Douglas, Miller, and Lamb (2025).

Suspended flocs were imaged through a 3 mm-thick flow-through slit built into the tank wall at the observation level. A DSLR fitted with a 5× microscope objective was aligned with the slit to record flocs as they crossed the narrow optical path, reducing intervening particles and improving clarity. This arrangement permits simultaneous control of mixing and imaging without interference from the drive assembly or external lighting.

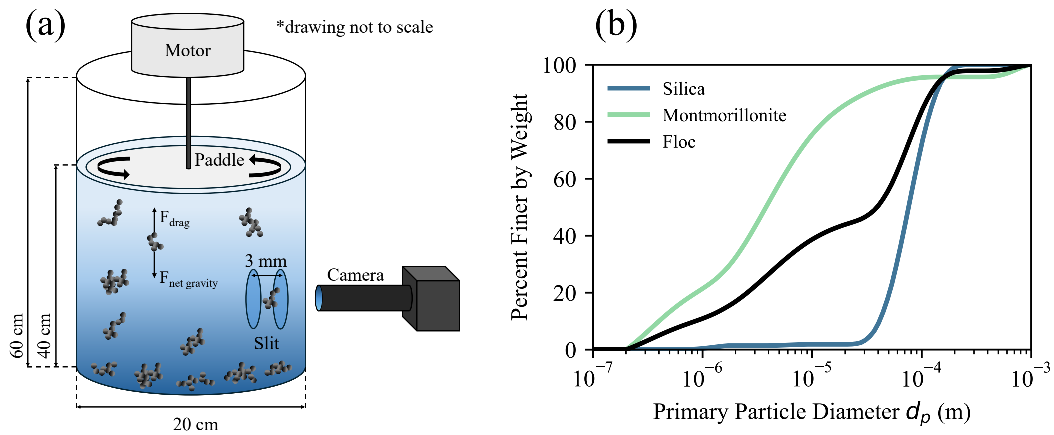

Figure 2.1: (a) Experimental apparatus. (b) Cumulative grain-size distributions of silica, montmorillonite, and flocs.

2.2 Experimental Runs

We conducted eight runs. Two calibration runs used lab spheres and silica grains to assess how particle shape influences settling and flocculation. The remaining six runs systematically varied shear velocity and particulate organic matter (POM) content to isolate their effects on floc formation and settling. Turbulent shear limits floc size by promoting breakup, whereas organic matter enhances aggregation by binding particles; controlling these variables therefore tests their respective roles in freshwater floc dynamics (Nghiem et al., 2022).

Each run used 10 g of solids: 5 g silica (SiO_2) and 5 g montmorillonite clay, a composition representative of natural aquatic sediments. Organic content was varied in three runs by adding guar gum—a plant-derived polysaccharide that mimics natural riverine organic matter—at 0, 1, or 2 wt %. For example, 1 wt % organic matter corresponds to 0.1 g guar gum per 10 g of solids. Shear velocity was adjusted in three additional runs to probe its effect on floc properties. Full experimental conditions, including organic-matter fraction and imposed u_*, are listed in Table 2.1.

Grain-size distributions for the silica and montmorillonite end-members were measured with a Camsizer and a Mastersizer, respectively (Fig. 2.1b). Together they span almost three orders of magnitude, with primary-particle diameters from 1×10^{-7}

Table 2.1: Summary of experimental conditions.

Exp Num	Experiment Type	POM (%)	Shear (m/s)
1	Lab Sphere	NA	NA
2	Silica	NA	NA
3	Floc Shear 1	2	0.02
4	Floc Shear 2	2	0.03
5	Floc Shear 3	2	0.04
6	Floc POM 1	1	0.04
7	Floc POM 2	2	0.04
8	Floc POM 3	3	0.04

m to 1×10^{-4} m (percent finer by mass). For the mixed-floc runs, we computed a composite distribution as the 50:50 mass-weighted average of the two mineral curves.

2.3 Image Processing Methods for Floc Velocity and Diameter

Analysis began with every frame of the recorded video sequence. Each frame was converted to grayscale, and a time-averaged image built from multiple frames was subtracted to remove the background (Fig. 2.2a). Particle boundaries were then detected from intensity gradients. To exclude poorly resolved images, we required that candidates exceed thresholds in both Laplacian variance and intensity standard deviation; accepted particles are highlighted in red in Fig. 2.2b (after S. J. Smith and Friedrichs, 2015).

We tracked in-focus particles frame-to-frame to obtain settling velocities. For a particle in frame i, a radius search located matches in frame $i+1$. Potential matches were scored on diameter consistency and Laplacian variance, weighted equally; tracking terminated if no candidate satisfied both thresholds (Fig. 2.2b).

Frame-to-frame displacements give raw velocities, but these include background flow. To isolate the gravitational component, we applied particle-image velocimetry (PIV) to a digitally filtered sequence that retained only tracers smaller than 10 μm, which faithfully follow the local flow (Fig. 2.2c). Subtracting this PIV-derived field from each tracked velocity yielded the true settling velocity (Fig. 2.2d; gray arrow = raw, white arrow = corrected).

After velocity correction, we derived diameters from projected areas. Binary masks isolated each particle, boundaries were traced, and a concave-hull algorithm accommodated irregular floc shapes. The enclosed area was then converted to an

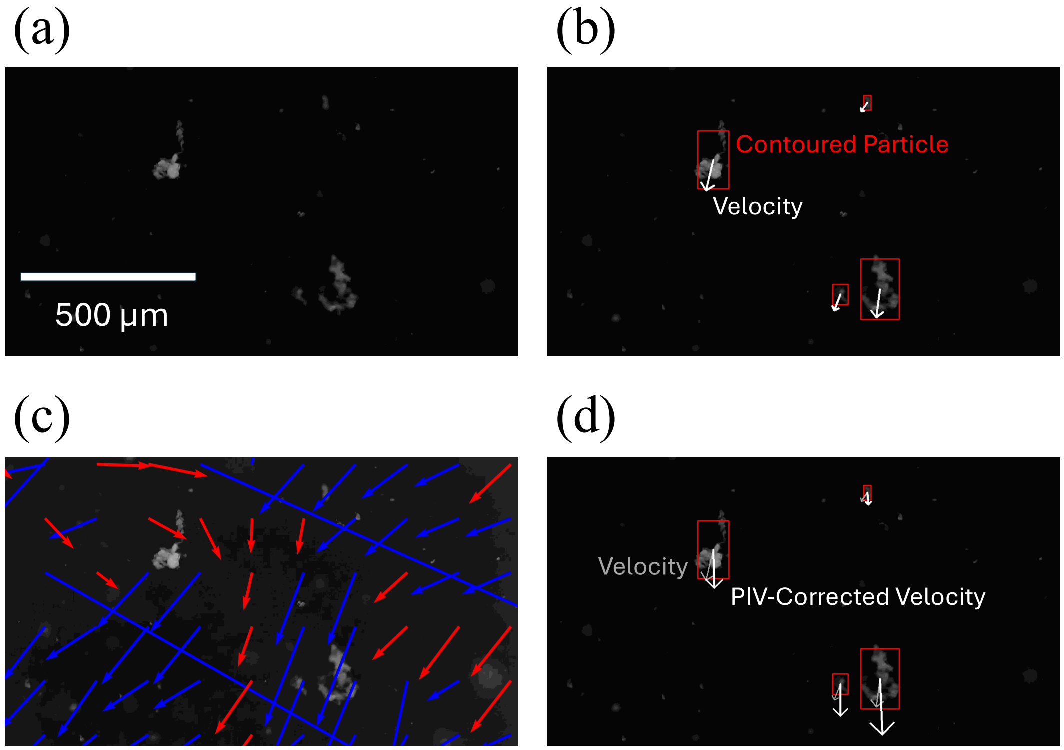

Figure 2.2: (a) Background-subtracted image, (b) contoured particle with raw velocity, (c) PIV, (d) contoured particle with gravitational settling velocity.

equivalent-circle diameter, which we used for subsequent log–log analyses.

2.4 Calibration and Settling Behavior Analysis

System calibration began with Experiments 1 and 2, which measured the settling of laboratory spheres (50 μm) and natural silica grains (Fig. 2.3a). Settling velocities were fitted with Stokes' law (Eq. (1.1)), treating the shape factor b_1 as a free parameter. For the spheres, the best-fit $b_1 = 17.7$ agrees closely with the theoretical value of 18 (Fig. 2.3b). Silica grains settled more slowly, giving $b_1 = 29.2$, a drag increase attributable to their angular, non-spherical shapes; Ferguson and Church (2004) reported a comparable $b_1 \approx 24$ for natural sediments of similar morphology.

Flocs settled even more slowly than silica and displayed far greater velocity scatter at any given diameter (Fig. 2.3b). Their reduced velocities reflect lower effective density and highly porous, irregular structures. Consequently, the velocity–diameter relation for flocs cannot be captured by a single shape factor. Instead, Eq. (1.4) combines Stokes' law with fractal scaling, introducing the floc fractal dimension n_f and the primary-particle diameter d_p to describe their behavior.

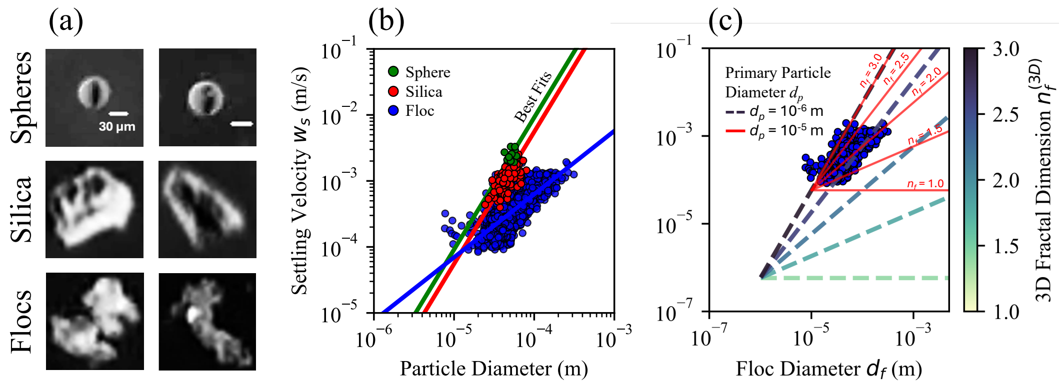

Figure 2.3: (a) Images of laboratory sphere, silica, and flocs. (b) Settling velocity fits for spheres, silica, and flocs. (c) Effect of varying primary particle diameter (d_p) on inferred fractal dimension.

Directly fitting Eq. (1.4) to the floc data is problematic because the primary-particle diameter, d_p, is unknown in natural samples and may vary by several orders of magnitude. Its assumed value exerts a strong influence on the inferred fractal dimension n_f (Fig. 2.3c): $d_p = 1 \times 10^{-6}$ m yields $n_f = 2.77$; $d_p = 1 \times 10^{-5}$ m gives $n_f = 2.10$; and $d_p = 1 \times 10^{-4}$ m produces $n_f = 3.00$.

To avoid this sensitivity, n_f is instead estimated from the log–log slope of settling velocity versus diameter, a measure that is independent of d_p. The bulk slope for the entire floc population is 1.9 (Fig. 2.3b). Bulk regression, however, can be biased by Simpson's paradox when the population is structurally heterogeneous, so flocs are first stratified by their *in-situ* image-based fractal dimension and slopes are computed for each subgroup separately.

2.5 Estimating Fractal Dimension of Flocs from 2D Projections

Accurately determining the three-dimensional (3D) fractal dimension from two-dimensional (2D) projections is fundamentally challenging, as the projection process ($\mathbb{R}^3 \rightarrow \mathbb{R}^2$) distorts essential geometric information about the aggregate. Additionally, our experimental setup employs a 3 mm-wide slit flow cell to minimize wall drag effects; however, this configuration introduces optical variability, since flocs are dispersed throughout the depth of the cell rather than constrained to a single focal plane. As a result, the captured images include particles at varying degrees of focus. Any method used to estimate the fractal dimension must therefore account for the geometric distortion introduced by projection and remain robust to image degradation and optical variability.

In principle, fractal theory (Eq. (1.2)) allows the fractal dimension to be inferred from the primary particle diameter (d_p) and the number of primary particles (N) comprising a floc. However, in natural settings, neither d_p nor N is constant or directly measurable *in situ*. As a result, a variety of *in situ* methods have been proposed to estimate floc fractal dimensions from observable image properties.

The *perimeter–area method* has previously been used to estimate the two-dimensional fractal dimension of flocs (Maggi and J. Winterwerp, 2004; Tang and Federico Maggi, 2015; Lee and Kramer, 2004). This method relies on the empirical scaling relation:

$$n_f^{(2D)}{}_{\text{perimeter}} = 2\,\frac{\log P}{\log A} \tag{2.1}$$

where P is the measured perimeter and A is the projected area of the particle in the 2D image. This expression is derived by analogy to the Euclidean relation $P = kA^{d/2}$, which holds for smooth (non-fractal) boundaries with $d = 1$. The underlying assumption is that, for a fractal boundary, the exponent in this scaling law approximates the true fractal dimension. However, both mathematical analysis and geometric constructions (e.g., the Koch curve) demonstrate that this assumption breaks down for truly fractal sets (Frame, Mandelbrot, and Neger, 2025; Cheng, 1995). For such boundaries, the perimeter may diverge while the enclosed area remains finite, making the relation $P = kA^{d/2}$ mathematically inconsistent. As a result, the exponent $n_f^{(2D)}{}_{\text{perimeter}}$ does not reliably represent the true boundary fractal dimension unless the area dimension $D_A = 2$.

Box-counting, in contrast, provides a mathematically rigorous and more general means of estimating the fractal dimension for both boundaries and interiors (Foroutan-pour, Dutilleul, and D. L. Smith, 1999). A key advantage of box-counting is that it does not require knowledge of the primary particle size (d_p) or the number of constituent particles (N), making it particularly well-suited for natural flocs where these values are unknown or variable (Spencer et al., 2022; Bellouti et al., 1997). The box-counting dimension $n_f^{(2D)}{}_{\text{box-counting}}$ is determined by measuring how the number of occupied boxes $N(\epsilon)$ at a given scale ϵ varies with scale (Mandelbrot, 1967):

$$n_f^{(2D)}{}_{\text{box-counting}} = \frac{\log N(\epsilon)}{\log(1/\epsilon)}. \tag{2.2}$$

However, when analyzing objects with finite extent (*in situ* imaging), finite-size effects and image pixelation introduce sensitivity to the scaling range. For a digital image of $N \times N$ pixels, the practical range of box sizes (ϵ) spans from 1 pixel up to

N pixels. Reliable estimation of $n_f^{(2D)}{}_{\text{box-counting}}$ requires a sufficiently broad range of box sizes to establish a stable linear trend on a log–log plot of $N(\epsilon)$ versus $1/\epsilon$. If the image is too small, the limited scaling range can yield unstable or underestimated values of $n_f^{(2D)}{}_{\text{box-counting}}$. For example, a 20×20 pixel image offers only about 1.3 orders of magnitude in scale, which is insufficient for robust fitting and does not recover the expected $n_f^{(2D)}{}_{\text{box-counting}} = 2$ for a smooth circle (Fig. 2.4a). In contrast, a 100×100 pixel image spans two full orders of magnitude, generally providing 6–7 usable data points for regression and a more reliable estimate of $n_f^{(2D)}{}_{\text{box-counting}}$. Panel (b) of Fig. 2.4 shows examples for two experimental flocs at high image resolution, illustrating the application of the box-counting method to real data.

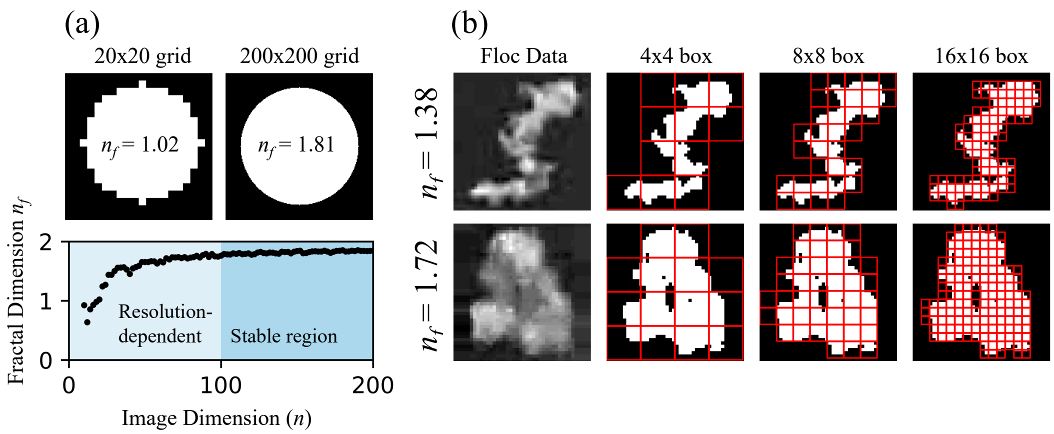

Figure 2.4: (a) Illustration of resolution dependency in box-counting dimension estimation using a perfect circle embedded in grids of 20×20 and 200×200 pixels, demonstrating that coarse grids systematically underestimate the fractal dimension. (b) Example box-counting dimension estimates for two experimental flocs imaged at $> 100 \times 100$ pixel resolution.

2.6 Estimating Primary Particle Diameter (d_p) from Settling Data

A key parameter in fractal settling models is the primary particle diameter (d_p), which sets the scale for both aggregate growth and density. Accurate estimation of d_p is essential for quantifying floc structure, interpreting settling data, and constraining physical models. However, d_p is rarely measured directly in natural or experimental settings, necessitating indirect inference from observable trends in the settling behavior of floc populations.

Using Eq. (1.4), the settling velocity of a floc is expressed as a power-law function of floc diameter, fractal dimension, and a drag/shape factor. When the floc population contains subgroups with distinct fractal dimensions, each group yields a separate log–log trend between settling velocity (w_s) and floc diameter (d_f). The intersection of these trends provides a means to estimate the effective primary particle diameter, d_p.

For two groups, j and k, with fractal dimensions $n_{f,j}$ and $n_{f,k}$ and drag/shape factors $b_{1,j}$ and $b_{1,k}$, the intersection diameter $d_{f,\mathrm{int}}$ is the floc diameter at which both groups predict the same settling velocity. This is given by

$$d_{f,\mathrm{int}} = d_p \left(\frac{b_{1,j}}{b_{1,k}} \right)^{1/(n_{f,j}-n_{f,k})} \tag{2.3}$$

which accounts for possible differences in drag/shape factor.

In the special case where $b_{1,j} = b_{1,k}$, this reduces to

$$d_{f,\mathrm{int}} = d_p \tag{2.4}$$

indicating that, for constant drag, all fitted lines intersect at the primary particle diameter.

In practice, we identify intersection points of the log–log settling velocity fits across floc subgroups and use the central tendency (such as the median) of these intersection diameters to estimate d_p for the sample. Systematic deviations of $d_{f,\mathrm{int}}$ from the known or expected primary particle size may indicate variation in the drag/shape factor or violations of model assumptions. The full algebraic derivation is provided in the appendix.

Chapter 3

RESULTS

This chapter presents our analysis of floc structure and settling dynamics. We first stratify the data by the two-dimensional box-counting fractal dimension, $n_f^{(2D)}$, and infer the corresponding three-dimensional fractal dimension, $n_f^{(3D)}$, from settling behaviour. We then extend this approach to the full floc data set to test the robustness of the 2-D–3-D relationship. Next, we compare the empirical conversion between $n_f^{(2D)}$ and $n_f^{(3D)}$ with theoretical and simulation-based models from the literature. Finally, we evaluate whether the primary-particle diameter, d_p, can be inferred from the fitted settling relations and discuss the physical assumptions and constraints that govern this method.

3.1 Stratifying 2D box-counting to infer 3d fractal dimension

We computed the two-dimensional box-counting fractal dimension, $n_f^{(2D)}$, for Experiment 3; values span 1.3–1.6. To test the impact of stratification, the data were divided into 3, 6, and 12 bins of $n_f^{(2D)}$. Within each bin we fitted a power-law relation between settling velocity, w_s, and floc diameter, d_f, in log–log space (Figs. 3.1a, d, g). The model $\log_{10}(w_s) = m \log_{10}(d_f) + b$ was calibrated with an ensemble Markov-chain Monte-Carlo sampler. After burn-in and thinning, the posterior medians of the slope, m, and intercept, b, were retained for further analysis. The slope m rises systematically as the binning becomes finer (Figs. 3.1b, e, h; red points). Because $w_s \propto d_f^{n_f - 1}$, each slope yields a three-dimensional fractal dimension of $n_f^{(3D)} = m + 1$.

Plotting the inferred three-dimensional fractal dimensions, $n_f^{(3D)}$, against the corresponding group-mean two-dimensional values, $n_f^{(2D)}$, reveals a clear linear relationship in the 3- and 6-bin cases ($R^2 = 0.99$ and $R^2 = 0.97$, respectively) and a weaker—though still positive—trend for the 12-bin case ($R^2 = 0.63$; Fig. 3.1c, f, i). These patterns show that finer stratification can expose internal structure, but once bin populations drop below about 50 particles the increased sampling noise degrades the fit. On this basis we adopt a bin width of 0.1, which balances structural resolution with statistical robustness and yields reliable estimates of $n_f^{(3D)}$.

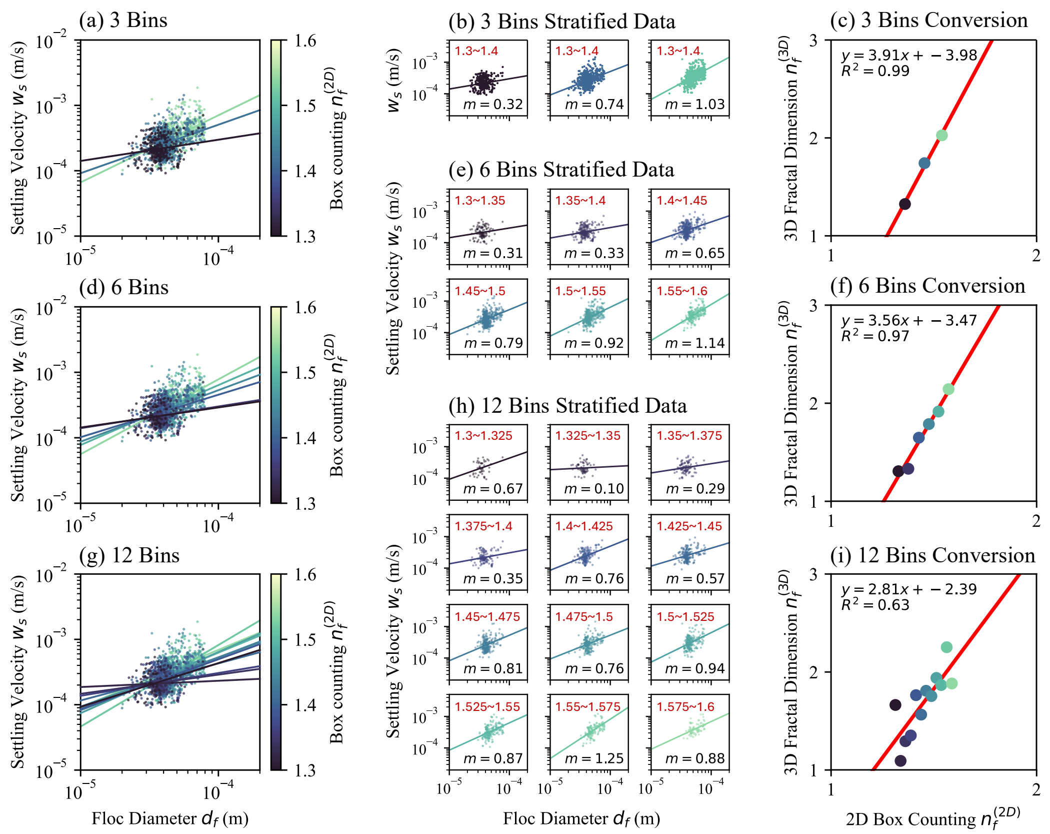

Figure 3.1: Stratification of floc data by 2D box-counting fractal dimension ($n_f^{(2D)}$). (a–c) Results using 3 bins: (a) log–log settling velocity vs. diameter with color-coded bins, (b) slope m for each bin, and (c) derived 3D fractal dimension ($n_f^{(3D)} = m + 1$) plotted against bin-averaged $n_f^{(2D)}$. (d–f) Same as above for 6 bins. (g–i) Same as above for 12 bins.

3.2 Inferring Fractal Dimension on All Floc Data

Using a bin width of 0.1, we analysed all floc data sets (Experiments 3–8), comprising three runs that varied shear velocity and three that varied particulate-organic-matter (POM) content. Only bins containing at least 50 particles were retained, restricting the usable range of $n_f^{(2D)}$ to 1.0–2.0 and yielding five to nine bins per experiment.

For each bin we fitted a power-law relation between settling velocity, w_s, and floc diameter, d_f, with an MCMC sampler and took the posterior-median slope, m. The corresponding three-dimensional fractal dimension is $n_f^{(3D)} = m + 1$. Inset panels in Fig. 3.2 plot $n_f^{(3D)}$ against the bin-averaged $n_f^{(2D)}$. Across all six experiments the stratified analysis yields a strong positive correlation, with high R^2.

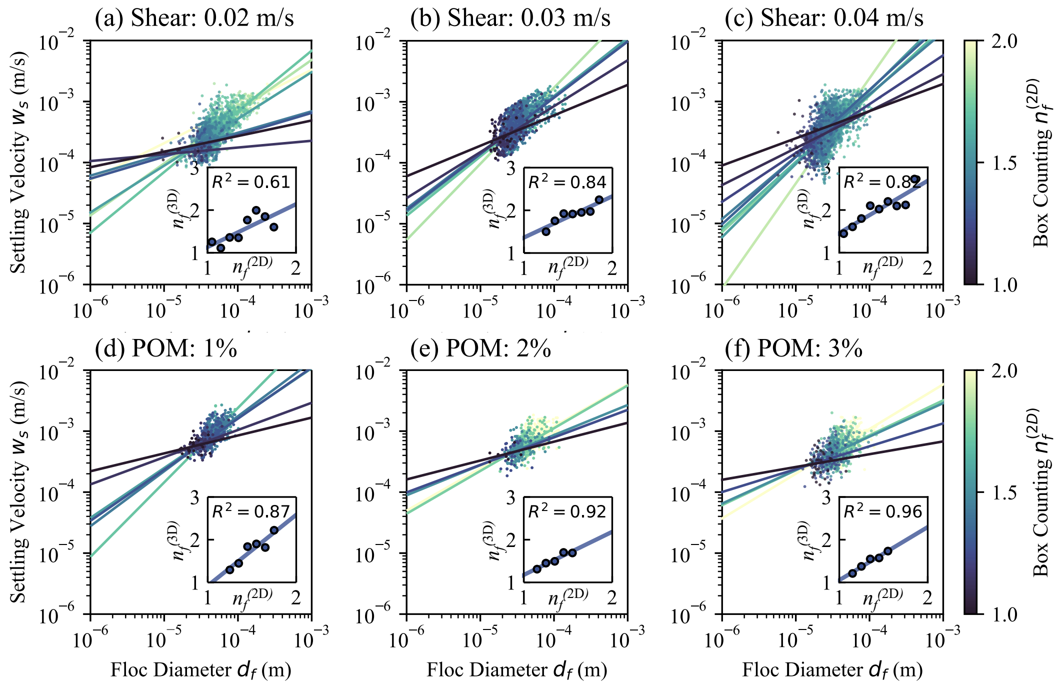

Figure 3.2: Comparison of stratified and aggregated fits for all floc datasets. (a–c) Varying shear velocity: 0.02, 0.03, and 0.04 m/s. (d–f) Varying POM content: 1%, 2%, and 3%. Inset plots show the relationship between $n_f^{(2D)}$ and slope-inferred $n_f^{(3D)}$ for each experiment.

We also examined the variability in inferred $n_f^{(3D)}$ across bins using the interquartile range (IQR), summarized in Table 3.1. The IQR values vary substantially across experiments, ranging from 0.083 to 0.248. Some datasets show tightly clustered values of $n_f^{(3D)}$, indicating high internal consistency (e.g., shear 0.03 m/s), while others exhibit wider spreads (e.g., shear 0.04 m/s and POM 3%), suggesting greater natural variability or sensitivity in slope estimates used to infer $n_f^{(3D)}$.

Table 3.1: Summary statistics of inferred 3D fractal dimension ($n_f^{(3D)}$) under different shear velocities and POM concentrations.

Condition	**Median**	**IQR**	**Q1 – Q3**
Shear 0.02 m/s	1.599	0.191	1.500 – 1.691
Shear 0.03 m/s	1.801	0.083	1.801 – 1.884
Shear 0.04 m/s	2.074	0.242	1.953 – 2.194
POM 1%	1.756	0.164	1.592 – 1.756
POM 2%	1.658	0.099	1.559 – 1.658
POM 3%	1.551	0.248	1.427 – 1.675

Next, we compare the stratified and bulk-fit estimates of the three-dimensional fractal dimension. The bulk fit corresponds to a single best-fit line applied to all data without using any $n_f^{(2D)}$ stratification—equivalent to fitting the model $\log_{10}(w_s) = m\log_{10}(d_f) + b$ across the full dataset. The comparison between stratified and bulk approaches is shown in Fig. 3.3.

When comparing fractal dimensions across experimental conditions, the stratified fits reveal an increasing trend in $n_f^{(3D)}$ with rising shear velocity, whereas the bulk fits do not exhibit a comparable pattern (Fig. 3.3a). As particulate organic matter (POM) content increases, both approaches show decreasing fractal dimensions. However, the stratified method consistently yields lower $n_f^{(3D)}$ values, typically 0.1 to 0.2 lower than the bulk fit (Fig. 3.3b).

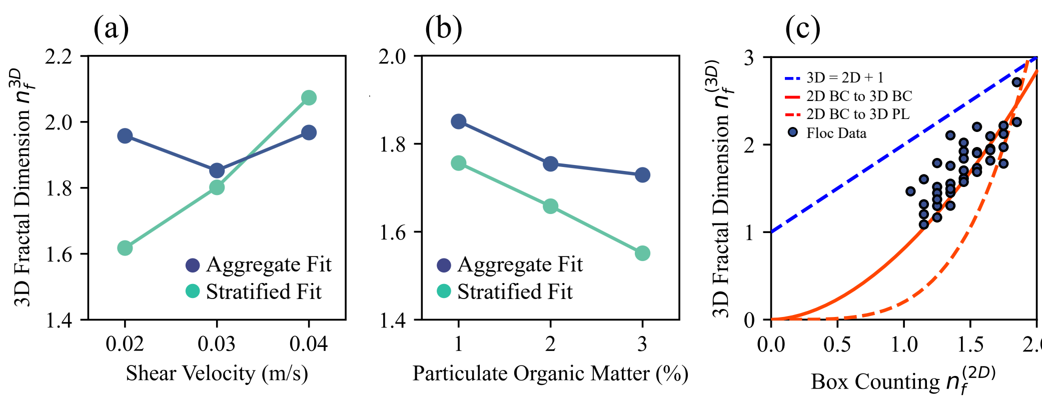

Figure 3.3: (a) Median inferred $n_f^{(3D)}$ versus shear velocity. (b) Median $n_f^{(3D)}$ versus POM content. (c) Relationship between $n_f^{(2D)}$ and slope-inferred $n_f^{(3D)}$ across all six datasets. The blue dashed line shows the idealized linear model ($n_f^{(3D)} = n_f^{(2D)} + 1$); the red solid and dashed lines show the empirical box-counting (BC) and power-law (PL) conversions from R. Wang et al. (2022).

3.3 Comparing 2D and 3D Fractal Dimension Relationships

Figure 3.3c shows the relationship between the two-dimensional box-counting fractal dimension ($n_f^{(2D)}$) and the inferred three-dimensional fractal dimension ($n_f^{(3D)}$) for all six floc datasets analyzed in this study. Three reference curves are plotted for comparison. The blue dashed line indicates the idealized linear relationship for a filled structure, $n_f^{(3D)} = n_f^{(2D)} + 1$. The solid orange line represents the empirical 2D-to-3D box-counting conversion proposed by R. Wang et al. (2022), $n_{f,BC}^{(3D)} = 0.8118\left(n_f^{(2D)}\right)^{1.8054}$. The dashed orange line shows the empirical power-law (mass–size scaling) conversion, $n_{f,PL}^{(3D)} = 0.2015\left(n_f^{(2D)}\right)^{4.079}$, also from R. Wang et al. (2022).

The experimental floc data fall between the empirical box-counting and power-law model curves, with most points aligning more closely with the 2D-to-3D box-counting conversion. Across the observed range of $n_f^{(2D)}$, the idealized linear relationship systematically overestimates $n_f^{(3D)}$. Both empirical models capture the observed increase in $n_f^{(3D)}$ with increasing $n_f^{(2D)}$, but the box-counting conversion provides the closest fit to the measured data.

3.4 Inferring Primary Particle Diameter (d_p)

To estimate the primary particle diameter (d_p), we used a Bayesian approach to quantify uncertainty in the intersection method. For each stratified floc group, we drew samples from the posterior distribution of the log–log settling velocity fits, and computed all pairwise intersections between fits from different groups using Eq. (2.4) (assuming a constant shape factor, b_1).

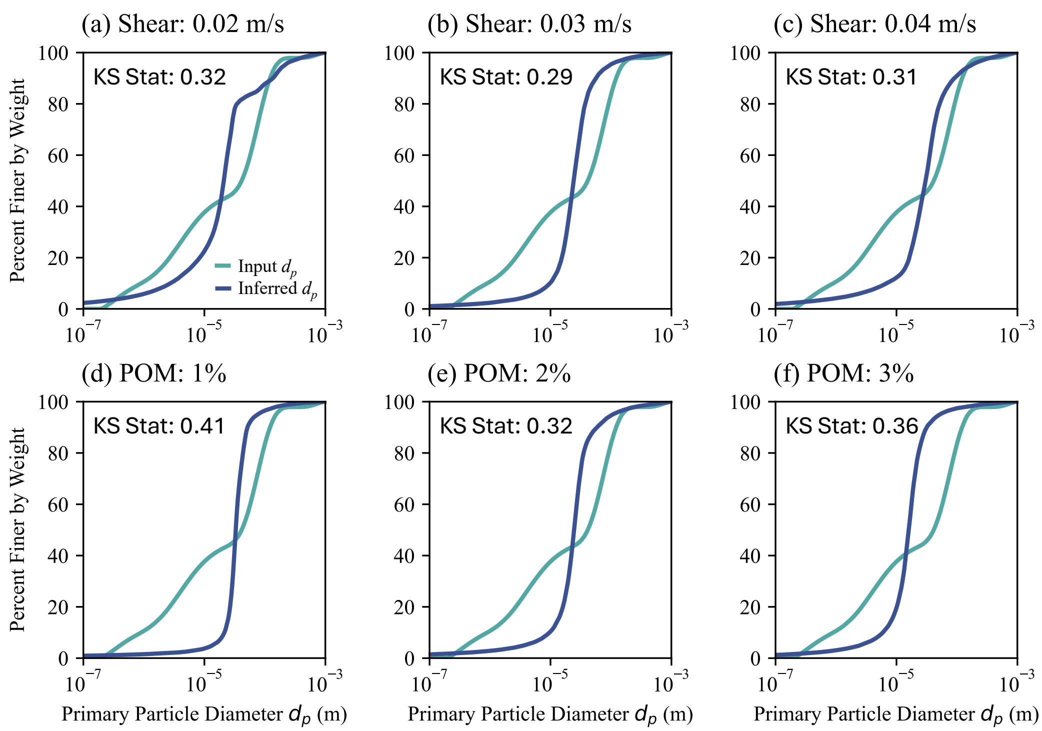

Figure 3.4: Cumulative percent finer by weight distributions comparing known input and inferred primary particle diameters (d_p) for all experiments. Panels show (a–c) varying shear velocity and (d–f) varying POM content. The Kolmogorov-Smirnov (KS) statistic quantifies the agreement between the two distributions in each panel.

Figure 3.4 compares the cumulative percent finer by weight distributions for both the known input particle sizes and the inferred d_p from the intersection approach. The Kolmogorov-Smirnov (KS) statistic, reported in each panel, provides a quantitative measure of agreement between the input and inferred distributions, with lower values indicating better fit. Across all six experimental conditions, the KS statistic ranges from 0.29 to 0.41. This indicates moderate agreement in the central tendency (e.g., the medians align well), but notable discrepancies in the tails and overall spread—particularly in experiments with higher POM content.

To address variability in the shape factor among fractal groups, we apply Eq. (2.3) so that the intersection diameter becomes a function of the primary particle diameter (d_p), shape factor (b_1), and fractal dimension (n_f). Previous studies, including those by Strom and Keyvani (2011), suggest that b_1 increases as n_f increases. For example, if b_1 rises from 10 to 100 across fractal dimensions, the resulting intersection diameter $d_{\text{intersect}}$ can be an order of magnitude larger than the true d_p for a fixed n_f. Conversely, if b_1 decreases with n_f, $d_{\text{intersect}}$ may be an order of magnitude smaller than d_p.

To illustrate the effect of the shape factor, we plot settling velocity versus diameter for two fractal groups ($n_f = 1.5$ and $n_f = 2.0$), both with a common primary particle diameter of 10 μm, using Eq. (1.4) (Fig. 3.5a). For $n_f = 1.5$, we fix $b_1 = 50$, and for $n_f = 2.0$, we vary b_1 from 10 to 100. As the shape factor increases with fractal dimension, the intersection diameter $d_{\text{intersect}}$ between the two groups becomes greater than the true primary particle diameter. The opposite holds if b_1 decreases with n_f.

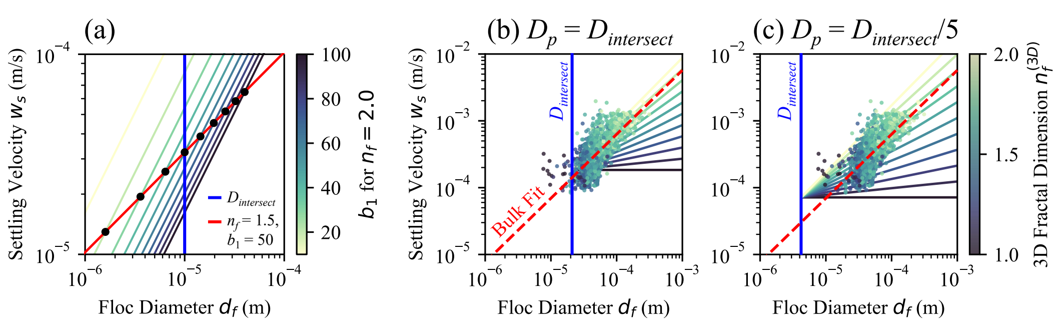

Figure 3.5: (a) Illustration of how varying b_1 with fractal dimension affects the intersection diameter $d_{\text{intersect}}$ for two fractal groups. (b) Data plotted with the intersection diameter found using previous methods, showing most measurements lie to the right of $d_{\text{intersect}}$. (c) Example where $d_p = d_{\text{intersect}}/5$.

We plot our data with the intersection diameter found using previous methods in

Fig. 3.5b and find that most of the measured diameters lie to the right of $d_{\text{intersect}}$. Based on theory, since the primary particle diameter represents the smallest constituent in the system, the intersection must logically occur to the left of all measured particle diameters. Therefore, only scenarios where $d_p < d_{\text{intersect}}$ are physically plausible.

This constraint implies a necessary relationship between b_1 and n_f: to maintain $d_p < d_{\text{intersect}}$ as n_f increases, b_1 must also increase. This requirement ensures that the primary particle remains the smallest size class in the system. Such a trend is consistent with both theoretical expectations and experimental observations, which suggest that denser, less permeable flocs (i.e., those with higher n_f) experience greater drag, corresponding to higher values of b_1.

Chapter 4

DISCUSSION

A central finding of this research is the discrepancy between fractal dimensions derived from aggregated datasets versus those derived from datasets stratified by 2D fractal dimension. As illustrated by our conceptual model (Fig. 1.1) and confirmed by experimental results (Figs. 3.2, 3.3), aggregating data from a floc population with inherent structural variability (i.e., a range of true n_f values) can lead to a bulk-fitted n_f that does not accurately represent any constituent subgroup. This is best described using Simpson's Paradox, where a trend apparent in different groups of data disappears when these groups are combined. In the context of floc settling, if larger flocs also tend to have higher fractal dimensions (due to different aggregation mechanisms or resilience to shear), an aggregated analysis can yield higher n_f. The stratified approach, by binning flocs based on their measured 2D box-counting fractal dimension, mitigates this issue, revealing more accurate relationships between floc structure and settling velocity.

4.1 Effect of Shear Velocity and Particulate Organic Matter (POM)

We observed an increasing trend in the inferred n_f with increasing shear velocity (Fig. 3.3), particularly when using the stratified analysis. This suggests that higher shear conditions may preferentially break up more tenuous, lower-n_f flocs, or lead to the formation of more compact, restructured aggregates that are more resistant to shear. This agrees with the literature as Winterwerp (1998) found n_f of 1.4 for very fragile floes, like marine snow, and about 2.2 for strong estuarine floes. The aggregated data, in contrast, showed little systematic trend, highlighting the potential risk of aggregating heterogeneous flocs to discern underlying physical processes.

Increasing POM content led to a decrease in the inferred n_f for both aggregated and stratified approaches, though stratified values were consistently lower (Fig. 8). This aligns with the understanding that organic matter, particularly extracellular polymeric substances (EPS), can act as a "glue," binding particles into larger, more open, and potentially more voluminous structures with lower fractal dimensions (Nghiem et al., 2022). These lower-n_f flocs, while potentially larger, would have a lower excess density for a given size, influencing their settling dynamics.

We describe these trends qualitatively, as numerous factors influence the observed relationships, including the specific experimental setup, the magnitude and duration of applied shear, and the composition and properties of the sediment.

4.2 2D to 3D Conversion of Fractal Dimension

The observed relationship between the 2D box-counting fractal dimension ($n_f^{(2D)}{}_{\mathrm{BC}}$) and the inferred 3D fractal dimension ($n_f^{(3D)}$) is broadly consistent with recent empirical models developed for synthetic aggregates, but departs from the predictions of classical fractal theory. The empirical 2D-to-3D box-counting mapping (R. Wang et al., 2022) best describes the experimental floc data, while the power-law scaling model is not fundamentally excluded, as most data points fall between these two curves. The idealized linear conversion ($n_f^{(3D)} = n_f^{(2D)} + 1$) consistently overestimates the 3D dimension across the measured range.

The modest deviation from the power-law scaling is likely a result of the variability in primary particle size in natural floc populations, which violates the constant d_p assumption required by classical theory. In both laboratory and field environments, d_p is not fixed but spans several orders of magnitude. In addition, natural flocs exhibit greater structural heterogeneity and porosity than synthetic aggregates, and the limitations of image resolution and sample size introduce further uncertainty.

Despite these challenges, the 2D box-counting dimension remains a practical and robust parameter for analyzing floc structure. It enables reproducible grouping of flocs and supports inference of the hydrodynamically relevant 3D dimension. Using $n_f^{(2D)}{}_{\mathrm{BC}}$ as a stratification parameter helps preserve structural variability, reduces aggregation bias in regression analysis, and improves the reliability of parameter estimates. This approach is therefore well suited for environments where sediment size and floc structure are highly variable, and enables quantitative linkage between image-based measurements and sediment transport modeling.

4.3 Constraining Primary Particle Diameter (d_p) and Shape Factor (b_1)

The primary particle diameter (d_p) and the drag or shape factor (b_1) are key parameters in fractal settling theory, yet they are rarely measured directly in experimental or field studies. In this analysis, we estimate d_p by identifying the intersection of log–log settling velocity trends corresponding to each n_f bin (Fig. 3.4). In principle, as d_f approaches d_p, all floc populations should converge to the settling velocity characteristic of a single primary particle, regardless of fractal dimension. Thus, the intersection diameter, d_{int}, serves as a practical proxy for d_p in these models.

The intersection analysis yields a median d_{int} that agrees well with the median of the input sediment sizes, yet the inferred distribution is much narrower: about two orders of magnitude wide compared with nearly four orders in the feed material. Two explanations are possible. Either (i) the imaging system fails to capture the very smallest grains, biasing the estimate upward, or (ii) only a subset of the source material (coarse silt to fine sand) actually participates in forming the larger flocs that dominate our observations. The present data cannot fully distinguish between these scenarios.

The method also rests on an implicit assumption that b_1 is constant across all n_f classes (Eq. (2.4)). If b_1 varies with structure, Eq. (2.3) shows that d_{int} will deviate from d_p. Our analysis (Fig. 3.5) indicates that physically plausible intersections ($d_p \leq d_{\text{int}}$) require b_1 to increase, or at least remain unchanged, as n_f increases. This trend is consistent with theory and experiments: denser, less permeable flocs (higher n_f) experience greater form drag and therefore larger b_1 values (Strom and Keyvani, 2011).

Uncertainty in d_p propagates directly into floc settling models. Figure 2.3b demonstrates that the value of n_f inferred from Eq. (1.4) is highly sensitive to the choice of d_p. Although the slope-based estimate of n_f ($n_f = m + 1$) avoids assuming a particular d_p, predictive modeling ultimately requires specification of both parameters. Assigning a single representative d_p, such as the median grain size, may not capture the full variability of natural systems. In practice, the effective d_p relevant for flocculation can be both narrower in range and offset in value relative to the bulk sediment size distribution.

4.4 Implications

Many sediment transport models use a single representative value for the floc fractal dimension, often $n_f \simeq 2$, to simplify parameterization (Winterwerp, 1998; Winterwerp, 2002; Kranenburg, 1994). However, our results indicate that even in controlled laboratory settings, the interquartile range of $n_f^{(3D)}$ is 0.08–0.25, and broadens further with increased variability in shear stress and particulate organic matter (POM) (Fig. 3.3). Aggregating heterogeneous data into a single n_f value can produce statistically misleading results that fail to represent the behavior of any specific subgroup within the population.

The consequences of using an inaccurate value for n_f in sediment transport models are significant. For example, if the true n_f is 1.9 but a model assumes $n_f = 2.0$, the settling velocity for a floc with a diameter 50 to 200 times greater than its primary particle can be overestimated by 35% to 58%. Such discrepancies can substantially affect predictions of sediment deposition, accumulation rates, and contaminant transport.

Furthermore, our results show that n_f often increases systematically with floc size (d_f). As a result, applying a single, constant value of n_f across a heterogeneous floc population will misrepresent the actual size dependence of settling velocity and the underlying structural variability. This leads to systematic errors in model predictions. These findings highlight the need to resolve n_f as a function of floc size or environmental conditions, or at minimum, to use stratified analysis methods that better represent the diversity of floc structures observed in natural systems.

These results show that representing a heterogeneous floc population with a single, universal fractal dimension (n_f) can introduce systematic bias and lead to inaccurate predictions of sediment transport dynamics. To address this, we recommend that models of flocculation and fine sediment transport account explicitly for structural variability within the floc population.

First, practitioners should employ high-resolution *in-situ* imaging or other structure-sensitive methods to quantify floc heterogeneity. Characterizing individual floc structure enables direct measurement of descriptors such as the two-dimensional box-counting fractal dimension (${n_f^{(2D)}}_{\mathrm{BC}}$). Using such descriptors, the floc population can then be stratified into subgroups that share similar structural properties.

Within each subgroup, the relationship between settling velocity and floc diameter should be analyzed independently to infer the hydrodynamically relevant three-dimensional fractal dimension ($n_f^{(3D)}$). Incorporating the resulting distribution of $n_f^{(3D)}$ values—rather than a single mean value—into transport models can better represent the range of floc behaviors present under varying environmental conditions. Alternatively, parameterizing n_f as a function of floc size, shear, or particulate organic matter may also improve model accuracy.

As measurement techniques advance and new data become available, practitioners are encouraged to revisit and, if appropriate, revise the choice of stratification parameter or structural descriptor. Incorporating these approaches into sediment transport modeling will better capture natural variability in floc structure and improve the reliability of model predictions.

Chapter 5

CONCLUSIONS

This study demonstrates that accounting for heterogeneity within floc populations is essential for accurate sediment transport modeling. Aggregating settling data across flocs with varying fractal dimensions often produces misleading results due to Simpson's Paradox: trends present within structural subgroups can be lost or distorted when data are pooled. By stratifying flocs based on 2D box-counting fractal dimensions, we resolve these structural differences, enabling more physically meaningful inference of transport parameters.

The stratified approach introduced here consistently reveals underlying physical trends that are obscured by aggregation. We find that the hydrodynamically inferred three-dimensional fractal dimension (n_f) increases with shear stress—indicative of more compact, resilient aggregates—and decreases with increasing particulate organic matter (POM) content, which favors the formation of larger, more open structures. Our work establishes a robust empirical relationship between 2D and 3D fractal dimensions that is more consistent with experimental data than theoretical conversions based on synthetic aggregates. In addition, we present a method to constrain the effective primary particle diameter (d_p) and show that the drag or shape factor (b_1) must increase with fractal dimension for models to remain physically consistent.

The key implication is that the widespread practice of using a single, representative fractal dimension (e.g., $n_f \approx 2.0$) in sediment transport models is a critical oversimplification. Even modest structural variability can result in significant predictive errors. As demonstrated here, a 0.1 difference in n_f can alter settling velocity estimates by 35–58% for realistic floc size ranges, with substantial impacts on predictions of sediment deposition and contaminant transport.

Based on these findings, we recommend that practitioners move beyond single-value parameterizations of floc fractal dimension in sediment transport models. Instead, models should incorporate a distribution of n_f values that reflect both environmental conditions and the structural diversity of flocs. The hybrid, stratified method outlined in this study—using *in-situ* imaging to group flocs and infer hydrodynamically relevant three-dimensional fractal dimensions within each group—provides a practical approach for capturing this variability. At a minimum, models should include uncertainty quantification that reflects the sensitivity of the floc settling equation to n_f. Adopting structure-resolved or uncertainty-aware methods is crucial for improving predictions of sediment transport, delta evolution, and coastal response to environmental change.

BIBLIOGRAPHY

Aalto, Rolf, J Wesley Lauer, and William E Dietrich (2008). "Spatial and temporal dynamics of sediment accumulation and exchange along Strickland River floodplains (Papua New Guinea) over decadal-to-centennial timescales". In: *Journal of Geophysical Research: Earth Surface* 113.F1.

Bellouti, M et al. (1997). "Flocs vs granules: differentiation by fractal dimension". In: *Water Research* 31.5, pp. 1227–1231.

Bianchi, Thomas S et al. (2024). "Anthropogenic impacts on mud and organic carbon cycling". In: *Nature Geoscience* 17.4, pp. 287–297.

Bird, RD (2006). "Transport Phenomena Wiley". In: *Transport phenomena Wiley. 2nd edition*.

Cheng, Qiuming (1995). "The perimeter-area fractal model and its application to geology". In: *Mathematical Geology* 27, pp. 69–82.

Douglas, Madison M, Kimberly Litwin Miller, and Michael P Lamb (2025). "Mud cohesion governs unvegetated meander migration rates and deposit architecture". In: *Geological Society of America Bulletin* 137.1-2, pp. 522–540.

Droppo, Ian G (2001). "Rethinking what constitutes suspended sediment". In: *Hydrological processes* 15.9, pp. 1551–1564.

Droppo et al. (1997). "The freshwater floc: a functional relationship of water and organic and inorganic floc constituents affecting suspended sediment properties". In: *The Interactions Between Sediments and Water: Proceedings of the 7th International Symposium, Baveno, Italy 22–25 September 1996*. Springer, pp. 43–53.

Esposito, Christopher R et al. (2017). "Efficient retention of mud drives land building on the Mississippi Delta plain". In: *Earth Surface Dynamics* 5.3, pp. 387–397.

Family, Fereydoon and David P Landau (2012). *Kinetics of aggregation and gelation*. Elsevier.

Ferguson, RI and M Church (2004). "A simple universal equation for grain settling velocity". In: *Journal of sedimentary Research* 74.6, pp. 933–937.

Foroutan-pour, Kayhan, Pierre Dutilleul, and Donald L Smith (1999). "Advances in the implementation of the box-counting method of fractal dimension estimation". In: *Applied mathematics and computation* 105.2-3, pp. 195–210.

Frame, Michael, Benoit Mandelbrot, and Nial Neger (2025). *Fractal Geometry*. `https://gauss.math.yale.edu/fractals/`. Yale University. Accessed: 2025-05-22. Yale University Department of Mathematics.

Hajek, Elizabeth A and Matthew A Wolinsky (2012). “Simplified process modeling of river avulsion and alluvial architecture: Connecting models and field data”. In: *Sedimentary Geology* 257, pp. 1–30.

Healy, Terry, Ying Wang, and J-A Healy (2002). *Muddy coasts of the world: processes, deposits and function*. Vol. 4. Elsevier.

Jarvis, Peter, Bruce Jefferson, and Simon A Parsons (2005). “Measuring floc structural characteristics”. In: *Reviews in Environmental Science and Bio/Technology* 4, pp. 1–18.

Johnson, Clifford P, Xiaoyan Li, and Bruce E Logan (1996). “Settling velocities of fractal aggregates”. In: *Environmental science & technology* 30.6, pp. 1911–1918.

Jullien, R (1987). “Aggregation phenomena and fractal aggregates”. In: *Contemporary Physics* 28.5, pp. 477–493.

Kemp, G Paul et al. (2016). “Enhancing mud supply from the Lower Missouri River to the Mississippi River Delta USA: Dam bypassing and coastal restoration”. In: *Estuarine, Coastal and Shelf Science* 183, pp. 304–313.

Kranenburg, Cees (1994). “The fractal structure of cohesive sediment aggregates”. In: *Estuarine, Coastal and Shelf Science* 39.5, pp. 451–460.

Lamb, Michael P et al. (2020). “Mud in rivers transported as flocculated and suspended bed material”. In: *Nature Geoscience* 13.8, pp. 566–570.

Lee, Chunwoo and Timothy A Kramer (2004). “Prediction of three-dimensional fractal dimensions using the two-dimensional properties of fractal aggregates”. In: *Advances in colloid and Interface Science* 112.1-3, pp. 49–57.

Li, Da Hong and Jerzy Ganczarczyk (1989). “Fractal geometry of particle aggregates generated in water and wastewater treatment processes”. In: *Environmental science & technology* 23.11, pp. 1385–1389.

Liss, Steven N et al. (1996). “Floc architecture in wastewater and natural riverine systems”. In: *Environmental science & technology* 30.2, pp. 680–686.

Maggi, F and JC Winterwerp (2004). “Method for computing the three-dimensional capacity dimension from two-dimensional projections of fractal aggregates”. In: *Physical Review E* 69.1, p. 011405.

Mandelbrot, Benoit (1967). “How long is the coast of Britain? Statistical self-similarity and fractional dimension”. In: *science* 156.3775, pp. 636–638.

Meakin, Paul (Oct. 1992). “Aggregation kinetics”. In: *Physica Scripta* 46.4, pp. 295–331. DOI: 10.1088/0031-8949/46/4/002.

Nghiem, Justin A et al. (2022). “A mechanistic model for mud flocculation in freshwater rivers”. In: *Journal of Geophysical Research: Earth Surface* 127.5, e2021JF006392.

Simpson, Edward H (1951). “The interpretation of interaction in contingency tables”. In: *Journal of the Royal Statistical Society: Series B (Methodological)* 13.2, pp. 238–241.

Smith, S Jarrell and Carl T Friedrichs (2015). “Image processing methods for in situ estimation of cohesive sediment floc size, settling velocity, and density”. In: *Limnology and Oceanography: Methods* 13.5, pp. 250–264.

Spencer, KL et al. (2022). “Quantification of 3-dimensional structure and properties of flocculated natural suspended sediment”. In: *Water Research* 222, p. 118835.

Stokes, George Gabriel et al. (1851). “On the effect of the internal friction of fluids on the motion of pendulums”. In.

Strom, Kyle and Ali Keyvani (2011). “An explicit full-range settling velocity equation for mud flocs”. In: *Journal of Sedimentary Research* 81.12, pp. 921–934.

Tang, Fiona HM and Federico Maggi (2015). “Reconstructing the fractal dimension of granular aggregates from light intensity spectra”. In: *Soft matter* 11.47, pp. 9150–9159.

Wang, Rui et al. (2022). “Fractal analysis of aggregates: Correlation between the 2D and 3D box-counting fractal dimension and power law fractal dimension”. In: *Chaos, Solitons & Fractals* 160, p. 112246.

Winterwerp (1998). “A simple model for turbulence induced flocculation of cohesive sediment”. In: *Journal of hydraulic research* 36.3, pp. 309–326.

– (2002). “On the flocculation and settling velocity of estuarine mud”. In: *Continental shelf research* 22.9, pp. 1339–1360.

Appendix A

DERIVATION OF d_p FROM SETTLING VELOCITY INTERSECTIONS

We begin with the general settling velocity law for a floc with primary particle diameter d_p, floc diameter d_f, three-dimensional fractal dimension n_f, and drag/shape factor b_1:

$$w_s = \frac{gR_s}{b_1 \nu d_p^{n_f-3}}\, d_f^{n_f-1} \tag{A.1}$$

Consider two subgroups, j and k, each characterized by different fractal dimensions $n_{f,j}$ and $n_{f,k}$, and potentially different drag factors $b_{1,j}$ and $b_{1,k}$. Their settling velocity laws are:

$$w_{s,j} = \frac{gR_s}{b_{1,j}\nu\, d_p^{n_{f,j}-3}}\, d_f^{n_{f,j}-1} \tag{A.2}$$

$$w_{s,k} = \frac{gR_s}{b_{1,k}\nu\, d_p^{n_{f,k}-3}}\, d_f^{n_{f,k}-1} \tag{A.3}$$

The intersection of these two relationships is given by the value $d_{f,\mathrm{int}}$ where $w_{s,j} = w_{s,k}$. Setting the two equations equal:

$$\frac{gR_s}{b_{1,j}\nu\, d_p^{n_{f,j}-3}}\, d_{f,\mathrm{int}}^{n_{f,j}-1} = \frac{gR_s}{b_{1,k}\nu\, d_p^{n_{f,k}-3}}\, d_{f,\mathrm{int}}^{n_{f,k}-1} \tag{A.4}$$

Cancelling common factors (gR_s and ν):

$$\frac{1}{b_{1,j} d_p^{n_{f,j}-3}}\, d_{f,\mathrm{int}}^{n_{f,j}-1} = \frac{1}{b_{1,k} d_p^{n_{f,k}-3}}\, d_{f,\mathrm{int}}^{n_{f,k}-1} \tag{A.5}$$

Rearranging:

$$d_{f,\mathrm{int}}^{n_{f,j}-1} \cdot b_{1,k} d_p^{n_{f,k}-3} = d_{f,\mathrm{int}}^{n_{f,k}-1} \cdot b_{1,j} d_p^{n_{f,j}-3} \tag{A.6}$$

$$d_{f,\mathrm{int}}^{n_{f,j}-n_{f,k}} = \frac{b_{1,j}}{b_{1,k}} d_p^{n_{f,j}-n_{f,k}} \tag{A.7}$$

$$\left(\frac{d_{f,\mathrm{int}}}{d_p}\right)^{n_{f,j}-n_{f,k}} = \frac{b_{1,j}}{b_{1,k}} \tag{A.8}$$

Taking both sides to the power $1/(n_{f,j} - n_{f,k})$ gives:

$$\frac{d_{f,\mathrm{int}}}{d_p} = \left(\frac{b_{1,j}}{b_{1,k}}\right)^{1/(n_{f,j}-n_{f,k})} \tag{A.9}$$

$$d_{f,\mathrm{int}} = d_p \left(\frac{b_{1,j}}{b_{1,k}}\right)^{1/(n_{f,j}-n_{f,k})} \tag{A.10}$$

Special Case: Constant Drag/Shape Factor If $b_{1,j} = b_{1,k}$, the intersection reduces to:

$$d_{f,\mathrm{int}} = d_p \tag{A.11}$$

That is, when the shape factor is identical, all theoretical curves intersect at the primary particle diameter, independent of fractal dimension.

General Case: Variable Drag/Shape Factor If the drag/shape factor varies between groups, the intersection diameter is shifted by a factor depending on the ratio of drag coefficients and the difference in fractal dimensions:

$$d_{f,\mathrm{int}} = d_p \left(\frac{b_{1,k}}{b_{1,j}}\right)^{1/(n_{f,k}-n_{f,j})} \tag{A.12}$$

Here, the conventional ordering ($k > j$) ensures a positive exponent. This expression provides the basis for estimating the effective primary particle diameter or diagnosing variability in the drag factor when comparing floc groups with distinct fractal structure.